Tuning anti-Klein to Klein tunneling in bilayer graphene

Renjun Du (杜人君),[1,*] Ming-Hao Liu (劉明豪),[2,3] Jens Mohrmann,[1] Fan Wu (吳凡),[1,4] Ralph Krupke,[1,5] Hilbert v. Löhneysen,[1,6] Klaus Richter,[2] and Romain Danneau[1,†]

[1]*Institute of Nanotechnology, Karlsruhe Institute of Technology (KIT), D-76021 Karlsruhe, Germany*
[2]*Institut für Theoretische Physik, Universität Regensburg, D-93040 Regensburg, Germany*
[3]*Department of Physics, National Cheng Kung University, Tainan 70101, Taiwan*
[4]*College of Optoelectronic Science and Engineering, National University of Defense Technology, Changsha 410073, China*
[5]*Institute of Material Science, Technische Universität Darmstadt, D-64287 Darmstadt, Germany*
[6]*Institute for Solid State Physics and Physics Institute, Karlsruhe Institute of Technology (KIT), D-76021 Karlsruhe, Germany*

(Dated: May 2, 2018)

We report that in gapped bilayer graphene, quasiparticle tunneling and the corresponding Berry phase exhibit features of single layer graphene. The Berry phase is detected by a high-quality Fabry-Pérot interferometer based on bilayer graphene. We found that the Berry phase is continuously tuned from 2π to 0.34π in gapped bilayer graphene by raising the Fermi energy of charge carriers, in contrast to the Berry phase of 2π in pristine bilayer graphene. Particularly, a Berry phase of π, which is the standard value for single layer graphene, is also observed in gapped bilayer graphene. By analyzing the transmission probability of charge carriers at normal incidence, we demonstrate a transition from (nearly perfect) Klein tunneling, a typical phenomenon in single layer graphene, to broken anti-Klein tunneling, known in gapped bilayer graphene, by decreasing the Berry phase. The maximum transmission probability of 0.87, which is close to unity, indicates that complete Klein tunneling is achievable in gapped bilayer graphene.

Introduction. Bilayer graphene (BLG), like its single layer counterpart [1–4], exhibits outstanding physical properties [5–8] and is often regarded as promising materials for potential electronic applications. One striking feature of BLG is the possibility to induce and tune an electronic band gap by breaking the lattice inversion symmetry using, for example, an electric field [7–11]. However, the fundamental knowledge of the gapped states in BLG remains limited in many respects despite the existing studies of the Berry phase [6, 12–15] or quasiparticle tunneling [14, 16–18].

The emergence of a band gap has a strong impact on the Berry phase by modulating the pseudospin σ [19, 20], which expresses an extra quantum mechanical degree of freedom in graphene [1, 16]. In Figs. 1(a)–(b) the pseudospin vectors are represented by small cones, located between the conduction (yellow) and valence (blue) bands in the momentum space. After a pseudospin vector adiabatically travels a closed path around the valley, e.g., the red circle in Figs. 1(a)–(b), a Berry phase is acquired [15, 21, 22]. This process is better visualized on a Bloch sphere, as shown in Figs. 1(c)–(d), where the pseudospin (denoted by arrows) traces out a solid angle which is equivalent to the Berry phase of BLG [15, 21]. In the absence of a band gap, e.g., in pristine BLG, the pseudospin vector always lies in the plane [20] (see Figs. 1(a) and (c)), so the corresponding Berry phase always remains 2π [6, 8] as shown by the half-spherical surface in Fig. 1(c). On the other hand, the pseudospin may be polarized out of plane [15, 19, 20, 22, 23] in gapped BLG (see Figs. 1(b) and (d)), leading to a Berry phase in the range of 0–2π as shown in Fig. 1(d). The understanding of the tunable Berry phase in gapped BLG may shed light on the physical phenomena, such as the valley Hall effect [24–27], the anomalous Hall effect [28, 29], and quasiparticle tunneling [14, 15]. A comprehensive exploration of the Berry phase in gapped BLG is, therefore, of fundamental interest.

The band gap also significantly affects quasiparticle tunneling, which is associated with the pseudospin [16] and the Berry phase [14, 15]. The quasiparticle tunneling in pristine BLG exhibits perfect reflection when the charge carriers encounter a sharp potential barrier at normal incidence, effect known as anti-Klein tunneling [16, 18], as illustrated in Fig. 1(e). However, when the band gap opens, anti-Klein tunneling can be strongly reduced while the Berry phase slightly changes [14]. Indeed Klein tunneling, i.e., full transmission through a potential barrier [16, 17, 30–32], may be possible in

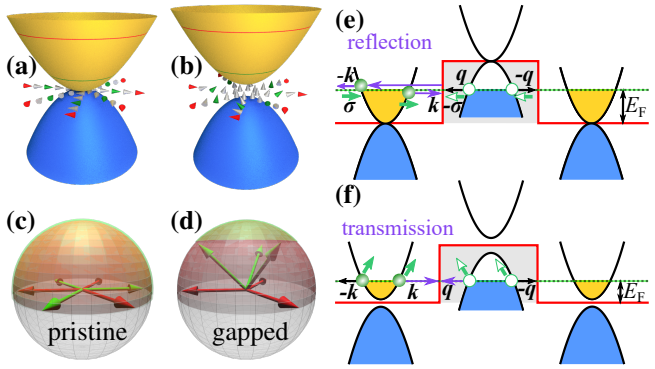

FIG. 1. Sketches of the pseudospin polarization for pristine (a) and gapped (b) BLG. The pseudospin is displayed as the small cones between the conduction (yellow) and valence (blue) bands. (c) and (d) show the corresponding Berry phase as the solid angle traced out by the pseudospin (arrows) on the Bloch sphere for (a) and (b), respectively. The red (green) color in (a)–(d) refers to the high (low) Fermi energy (E_F). (e) Anti-Klein tunneling for pristine BLG. k or q is the wave vector for electrons or holes. σ denotes the pseudospin. (f) Klein tunneling is possible in gapped BLG.

gapped BLG due to the out-of-plane polarization of the pseudospin [15] (Fig. 1(f)). However, the observation of Klein tunneling in gapped BLG requires low-disorder devices and ballistic transport. To the best of our knowledge, such an anti-Klein to Klein tunneling transition has not been observed in BLG.

In this paper, we employ an edge-connected hBN-BLG-hBN heterostructure (hBN for hexagonal boron nitride) to investigate quasiparticle tunneling in a lateral *pnp* junction. We benefit from an advanced sample fabrication method [33], yielding ultra-clean devices, which enable ballistic Fabry-Pérot (FP) interferences [34]. The phase-sensitive FP interference is used to detect the variation of the Berry phase. In contrast to previous work examining the Berry phase merely at high Fermi energies [14], the robust FP interference allows us to probe it close to the band edge. The role of the Berry phase and of the corresponding pseudospin on the quasiparticle tunneling will be discussed in detail and compared to numerical simulations based on a tight-binding model [35].

Sample description. The investigated devices, sketched in Fig. 2(a), consist of a hBN-BLG-hBN heterostructure. The encapsulation of BLG results in low-disorder devices, allowing ballistic transport over a distance of 9 µm. The potential profile across the device is controlled by a local top gate about 150 nm wide as well as a global back gate (Si substrate). The fabrication follows Ref. 33. Details of the devices are shown in Supplemental Material [36]. Each device is divided into four regions, labeled as T (top- and back-gated region), B (only back-gated regions), and C (contact-overlapping region) in Fig. 2(b). The overlapping contact results in additional *n*-doping in region C when both gates are set to zero, as displayed in Fig. 2(e), where the carrier density profile is obtained from finite-element-based electrostatic simulation using FEniCS [37] combined with the mesh generator Gmsh [38].

Fabry-Pérot interferences. The conductance (G) as a function of the top- ($V_{\rm tg}$) and back-gate ($V_{\rm bg}$) voltages has been probed experimentally and modeled for device PNJ-A, as shown in Figs. 2(c) and (d), respectively. The conductance minima appear as three lines in these plots. The two horizontal lines at $V_{\rm bg} \approx -1.3\,$V and $V_{\rm bg} \approx -26.9\,$V are independent of $V_{\rm tg}$, and indicate the charge neutrality point (CNP) in regions B and C, respectively. The position of the CNP is determined by the initial doping of each region (see Fig. 2(e)). The diagonal line shows the CNP of the dual-gated region T and defines the displacement field axis, along which the interlayer asymmetry develops. The three lines partition the map into six sections, each of which has a unique combination of charge carrier polarities, as labeled on Figs. 2(c)–(d).

In the bipolar regime ($n\bar{p}nn$, $p\bar{n}pn$ and $p\bar{n}pp$), where the charge carrier type in region T (denoted by the overlined symbol) is different from region B, we observe clear conductance oscillations as a consequence of FP interferences. The fringes extend along the diagonal line, illustrating that the interference occurs in a cavity tuned by both $V_{\rm tg}$ and $V_{\rm bg}$. The cavity length determined as in Ref. 14 is found to be around 150 nm,

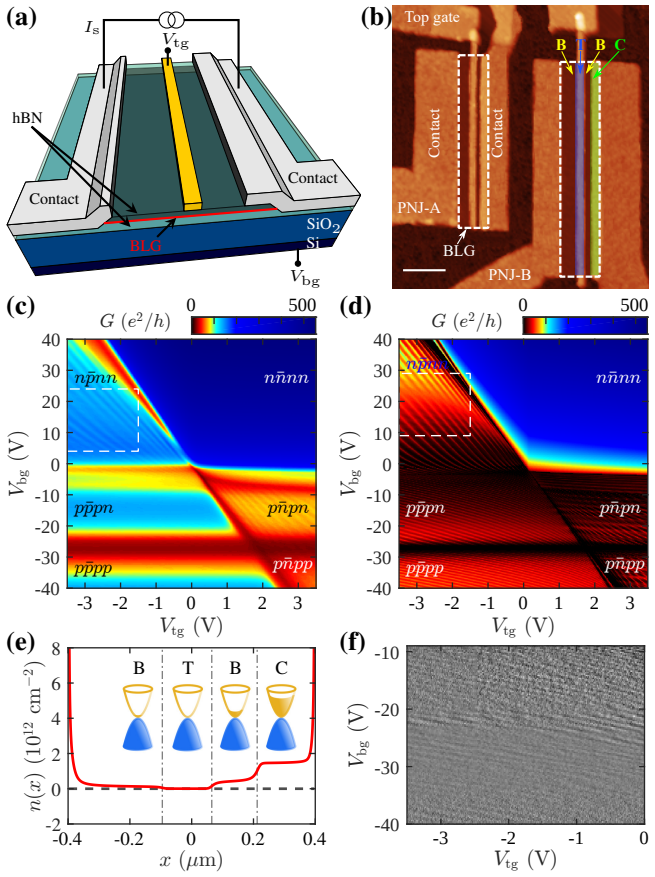

FIG. 2. Sketch (a) and AFM image (b) of the devices. Scale bar in (b) is 1 µm. Experimental (c) and simulation (d) results of conductance G varying with $V_{\rm tg}$ and $V_{\rm bg}$ at 4.2 K and zero magnetic field for device PNJ-A. (e) The initial charge carrier density $n(x)$ across device PNJ-A when $V_{\rm bg}$ and $V_{\rm tg}$ are both zero. (f) Transconductance $dG/dV_{\rm tg}$ in the $p\bar{p}pn$ and $p\bar{p}pp$ regions of (c).

which corresponds to the top-gate width. On the other hand, due to the long spacing between the contacts, FP interferences in unipolar regimes such as $p\bar{p}pn$ and $p\bar{p}pp$ are hardly visible. However, the weak oscillations become discernible in the transconductance $dG/dV_{\rm tg}$ gate map, see Fig. 2(f). More details about FP interferences are shown in Supplemental Material [36].

To gain further insight into the implications and ramifications of our experimental results, quantum transport simulations based on the real-space Green's function method using the tight-binding model for Bernal-stacked BLG has been performed. Details of the simulation method are similar to Ref. 14, including how the gate-tunable interlayer asymmetry parameter U can be implemented [8], with the following two alterations. First, the scalable tight-binding model [39] with a scaling factor of $s_f = 4$ has been adopted. Second, carrier density profiles obtained from electrostatic simulations [an example is shown in Fig. 2(e)] have been implemented in order to extract realistic on-site energy profiles for the tight-binding model Hamiltonian. More details about the gate-modulated carrier density profiles can be found in Supplemental Mate-

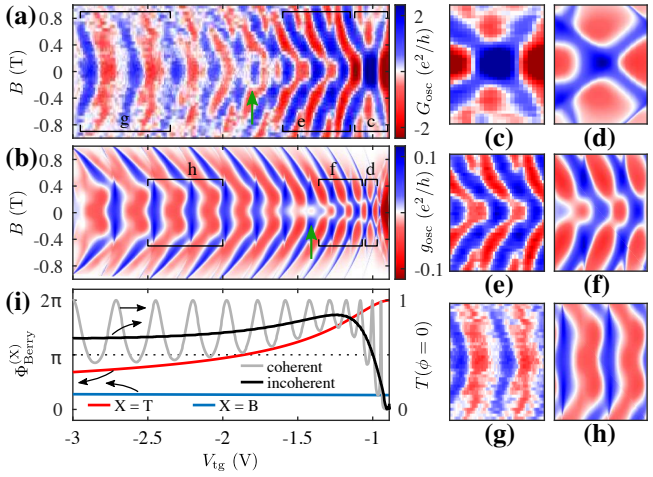

FIG. 3. Fabry-Pérot interference measurements (a) and simulations (b) at $V_{bg} = 20\,V$ under low magnetic fields for device PNJ-B (conductance measurements at zero magnetic filed are shown in Supplemental Material [36]). The Fabry-Pérot fringes in (a) and (b) show similar dispersion, despite certain scaling of the fringes in (b). The regions labeled by c–h are highlighted in the corresponding panels (c)–(h). (i) Berry phases for regions B and T are shown as blue and red curves, respectively. The corresponding transmission probability at normal incidence is calculated with phase-coherent (grey curve) and phase-incoherent (black curve) methods.

rial [36]. Comparing Figs. 2(c) and (d), our experiment captures all the interference patterns that are theoretically predicted. This agreement demonstrates the high quality of both our FP interferometer design and the quantum transport simulations, even comparable to the suspended graphene interferometer with smooth junction profiles that led to high FP finesse [34].

Berry phase at low magnetic fields. The phase-sensitive FP interference is utilized under low magnetic fields, where the quantum Hall effect has not yet emerged, in order to probe the Berry phase variation within the cavity. Figures 3(a) and (b) present the FP interference as a function of V_{tg} and B ($|B| \leq 1\,T$) at $V_{bg} = 20\,V$ for the experiment and simulation, respectively. To highlight the conductance oscillations, we subtract a smoothed background $G_0(V_{tg})$ (experiments) or $g_0(V_{tg})$ (simulations) at each B value, and obtain the oscillating part by $G_{osc} = G - G_0$ (experiments) or $g_{osc} = g - g_0$ (simulations). Here, g represents the calculated conductance without considering the conduction mode [35]. Comparing Figs. 3(a) and (b), the low-field dispersion of the FP fringes shows remarkable agreement between the experiment and simulation, despite certain scaling of the fringes in Fig. 3(b). For better comparison, the fringes in the regions labeled c–h are highlighted in Figs. 3(c)–(h). While decreasing V_{tg} from the CNP ($-0.89\,V$), the Fermi energy of charge carriers increases. For V_{tg} close to the CNP, the fringes experience a series of sudden shifts at $B \approx 0.1$–$0.3\,T$ (see Figs. 3(e) and (f)), which resembles the behavior of single-layer graphene (SLG) [30, 31, 40, 41]. The amount of shift increases up to half-period at $V_{tg} \approx -1.8\,V$ for the experiment and $V_{tg} \approx -1.4\,V$ for the simulation (see the green arrows in Figs. 3(a) and (b)), suggesting a phase change of π. For V_{tg} far away from the CNP, the fringes exhibit parabolic dispersion with respect to B as expected for BLG [14] (see Figs. 3(g) and (h)). We notice two distinct types of dispersion of FP fringes with B, i.e., the SLG-like phase shift at relative low Fermi energies (e.g., regions e and f) and the BLG-like parabolic dispersion at sufficiently high Fermi energies (e.g., regions g and h).

To interpret the observed phase shift in Fig. 3(a), we analyze the phase difference $\Delta\Phi$ between two neighboring transmitted waves. At low magnetic fields, $\Delta\Phi$ comprises three terms: the Wentzel-Kramers-Brillouin phase Φ_{WKB}, the Aharonov-Bohm phase Φ_{AB}, and the Berry phase Φ_{Berry}. Φ_{WKB} together with Φ_{AB} just yield a parabolic dispersion of the fringes with B [15]. Therefore, we calculate the Berry phase for regions T ($\Phi^{(T)}_{Berry}$) and B ($\Phi^{(B)}_{Berry}$) with the same gate range as used in the experiment (see Fig. 3(i)). The Berry phase in region B (blue curve) is affected by V_{bg} rather than V_{tg}, and takes a constant value of 0.28π for $V_{bg} = 20\,V$. On the contrary, the Berry phase in region T (red curve) decreases monotonically from 2π to 0.34π while V_{tg} drops from $-0.89\,V$ (CNP) to $-3\,V$. The evolution of the Berry phase in region T accounts well for the phase shift of FP interferences in the experiment. For $\Phi^{(T)}_{Berry} \geq \pi$, the strong variation of $\Phi^{(T)}_{Berry}$ coincides with the SLG-like phase shift. Particularly, the Berry phase in the T region crosses π at $V_{tg} = -1.86\,V$, which is in good agreement with the π-shift position in the experiment. In addition, the emergence of these phase shifts at certain magnetic fields illustrates that Φ_{Berry} arises in low magnetic fields, similar to the situation in SLG [30, 31]. On the other hand, for $\Phi^{(T)}_{Berry} < \pi$, the weakly reduced $\Phi^{(T)}_{Berry}$ corresponds to the BLG-like parabolic dispersion of the fringes, where the Berry phase has been picked up at zero magnetic field [14].

In order to understand the quasiparticle tunneling in gapped BLG, we investigated the transmission probability at normal incidence, $T(\phi = 0)$, as shown in Fig. 3(i). Two methods to calculate $T(\phi = 0)$ are considered: phase-coherent (grey curve) and phase-incoherent (black curve). The phase-coherent transmission probability oscillates for $V_{tg} \leq -0.89\,V$. Instead, the phase-incoherent transmission probability is calculated by the relation $T(\phi = 0) = 1/(1/T_L + 1/T_R - 1)$ [42], where T_L and T_R represent the transmission probability through the left and right *pn* interfaces of the potential barrier, respectively. The resulting phase-incoherent $T(\phi = 0)$ remains zero at the CNP, then surges to 0.87 at $V_{tg} = -1.24\,V$, and finally declines until ~ 0.65 with the reduction of V_{tg}. At the CNP, although $\Phi^{(T)}_{Berry}$ approaches the typical value, 2π, for anti-Klein tunneling, the suppress of transmission mainly attributes to the zero charge carrier density in region T. Here, two different types of quasiparticle tunneling are found. (i) Nearly perfect Klein tunneling. The maximum $T(\phi = 0)$ at $V_{tg} \approx -1.24\,V$ is close to the unity transmission probability for perfect Klein tunneling [16, 17, 30, 31]. (ii) The reduction of $T(\phi = 0)$ for $V_{tg} < -1.24\,V$ suggests that

anti-Klein tunneling is partially restored, leading to broken anti-Klein tunneling [14]. Therefore, the quasiparticle tunneling undergoes two processes: reaching Klein tunneling and recovering anti-Klein tunneling. The factor that impedes the maximum of $T(\phi = 0)$ to reach 1, is the Berry phase in region B because perfect Klein tunneling requires the Berry phase to be π in both T and B regions.

The results discussed above suggest that the transition from anti-Klein to Klein tunneling is achievable in gapped BLG. It is well known that the chirality sustains not only anti-Klein tunneling in pristine electronic BLG but Klein tunneling in SLG as well [16, 17]. On the contrary, Klein tunneling in gapped BLG favors the impaired chirality, which occurs due to the out-of-plane polarization of the pseudospin [15, 19, 20, 22] (see Fig. 1(b)). The momentum of charge carriers is, therefore, unlocked to the pseudospin, allowing Klein tunneling in gapped BLG (see Fig. 1(f)). On the other hand, the chirality as well as anti-Klein tunneling can be restored in gapped BLG [15]. As long as the Fermi energy is sufficiently high, the pseudospin recovers its in-plane orientation; at the same time, the Berry phase of 2π (or equivalently 0) is regained. The recovery of anti-Klein tunneling is affected by two parameters, namely, the interlayer asymmetry and the Fermi energy. The chirality is broken because of the increasing interlayer asymmetry but recovered due to the rising Fermi energy.

Phase shift of the FP fringe at zero magnetic field. Figures 4(a) and (b) show the FP interference patterns magnified from the white rectangles in Figs. 2(c) and (d), respectively. In the $n\bar{p}nn$ regime, we observe that the FP fringes exhibit nearly half-period shifts, for example, highlighted by the green-dashed lines in Figs. 4(a) and (b). The numerical simulation shows convincing agreement with our experimental finding. The nearly half-period shifts indicate the phase change of about π that abruptly adds to the phase difference $\Delta\Phi$ between two interfering trajectories. Since the FP interference occurs in the top-gated cavity, the origin of the phase jump lies in region T. On the other hand, the phase difference at $B = 0$ is only affected by the gate voltages, which modulate Φ_{Berry} to a large extent. Therefore, we calculate the Berry phase in region T as a function of V_{tg} and V_{bg} (see Fig. 4(c)), according to the interlayer asymmetry parameter U. In Fig. 4(c), the dash-dotted line shows the Berry phase of π in the $n\bar{p}nn$ regime. Below the π line, three green dots mark the phase-shift positions in Fig. 4(a), which arrange along the dotted line.

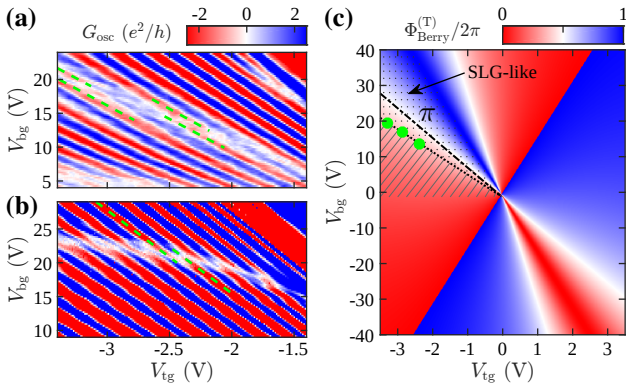

FIG. 4. Fabry-Pérot interferences at zero magnetic field are shown both experimentally (a) and theoretically (b), zoomed in the white rectangle of Figs. 2(c) and Fig. 2(d), respectively. (c) Calculation of the Berry phase in region T as a function of V_{tg} and V_{bg}. The dash-dotted line shows the position of $\Phi^{(\mathrm{T})}_{\mathrm{Berry}} = \pi$. The green dots mark the phase-shift positions occurred in (a), and define the dotted line.

The phase shifts of the FP fringes can be attributed to two different ways to acquire the Berry phase in gapped BLG. Below the dotted line (striped shade) in Fig. 4(c), $\Phi^{(\mathrm{T})}_{\mathrm{Berry}}$ is directly acquired at zero magnetic field as expected for BLG, and evolves towards π upon tuning V_{tg} and V_{bg}. But above the dotted line (dotted shade), $\Phi^{(\mathrm{T})}_{\mathrm{Berry}}$ fails to be picked up without the assistance of magnetic fields, which is a typical SLG-like behavior. Thus, the phase shifts about π show up around the dotted line.

Conclusion. We have examined the Berry phase in BLG using a Fabry-Pérot interferometer based on a dual-gated geometry. As the crystal inversion symmetry is broken by applying a displacement field, the Berry phase is fully controlled within 0.34π–2π by manipulating the Fermi energy of charge carriers. The related transmission probability at normal incidence shows that the quasiparticle tunneling is governed by two processes: reaching Klein tunneling and recovering anti-Klein tunneling. We obtain a maximum transmission probability of 0.87, illustrating that Klein tunneling is almost completely realized in gapped BLG. A transition from broken anti-Klein to almost complete Klein tunneling is clearly identified. Furthermore, switching between BLG-like anti-Klein tunneling and SLG-like Klein tunneling is reachable as long as the Berry phase over the device changes from 2π (or 0) to π by appropriate electrical gating.

We acknowledge A. Varlet for fruitful discussions. Financial supports from the Deutsche Forschungsgemeinschaft (DFG) within SFB 689 and the program of the Forschungsgroßgeräte 121384/17-1, the Helmholtz association through the program STN, as well as the DFG Center for Functional Nanostructures (CFN) are gratefully acknowledged.

* Renjun.Du@outlook.com
† romain.danneau@kit.edu

[1] K. S. Novoselov, A. K. Geim, S. V. Morozov, D. Jiang, M. I. Katsnelson, I. V. Grigorieva, S. V. Dubonos, and A. A. Firsov, Nature **438**, 197 (2005).
[2] A. K. Geim and K. S. Novoselov, Nat. Mater. **6**, 183 (2007).
[3] A. H. Castro Neto, F. Guinea, N. M. R. Peres, K. S. Novoselov, and A. K. Geim, Rev. Mod. Phys. **81**, 109 (2009).
[4] Y. Liu, G. Bian, T. Miller, and T.-C. Chiang, Phys. Rev. Lett. **107**, 166803 (2011).
[5] S. V. Morozov, K. S. Novoselov, M. I. Katsnelson, F. Schedin, D. C. Elias, J. A. Jaszczak, and A. K. Geim, Phys. Rev. Lett. **100**, 016602 (2008).

[6] K. S. Novoselov, E. McCann, S. V. Morozov, V. I. Fal'ko, M. I. Katsnelson, U. Zeitler, D. Jiang, F. Schedin, and A. K. Geim, Nat. Phys. **2**, 177 (2006).

[7] E. McCann, Phys. Rev. B **74**, 161403 (2006).

[8] E. McCann and M. Koshino, Rep. Prog. Phys. **76**, 056503 (2013).

[9] J. B. Oostinga, H. B. Heersche, X. Liu, A. F. Morpurgo, and L. M. K. Vandersypen, Nat. Mater. **7**, 151 (2008).

[10] Y. Zhang, T.-T. Tang, C. Girit, Z. Hao, M. C. Martin, A. Zettl, M. F. Crommie, Y. R. Shen, and F. Wang, Nature **459**, 820 (2009).

[11] T. Taychatanapat and P. Jarillo-Herrero, Phys. Rev. Lett. **105**, 166601 (2010).

[12] M. V. Berry, P. Roy. Soc. Lond. A Mat. **392**, 45 (1984).

[13] Y. Zhang, Y.-W. Tan, H. L. Stormer, and P. Kim, Nature **438**, 201 (2005).

[14] A. Varlet, M.-H. Liu, V. Krueckl, D. Bischoff, P. Simonet, K. Watanabe, T. Taniguchi, K. Richter, K. Ensslin, and T. Ihn, Phys. Rev. Lett. **113**, 116601 (2014).

[15] A. Varlet, M.-H. Liu, D. Bischoff, P. Simonet, T. Taniguchi, K. Watanabe, K. Richter, T. Ihn, and K. Ensslin, Phys. Status Solidi RRL **10**, 46 (2016).

[16] M. I. Katsnelson, K. S. Novoselov, and A. K. Geim, Nat. Phys. **2**, 620 (2006).

[17] M. I. Katsnelson, *Graphene: Carbon in Two Dimensions* (Cambridge University Press, 2012).

[18] V. Kleptsyn, A. Okunev, I. Schurov, D. Zubov, and M. I. Katsnelson, Phys. Rev. B **92**, 165407 (2015).

[19] H. Min, G. Borghi, M. Polini, and A. H. MacDonald, Phys. Rev. B **77**, 041407 (2008).

[20] A. H. MacDonald, J. Jung, and F. Zhang, Phys. Scripta **2012**, 014012 (2012).

[21] D. Xiao, M. C. Chang, and Q. Niu, Rev. Mod. Phys. **82**, 1959 (2010).

[22] M. B. Lundeberg and J. A. Folk, Science **346**, 422 (2014).

[23] P. San-Jose, E. Prada, E. McCann, and H. Schomerus, Phys. Rev. Lett. **102**, 247204 (2009).

[24] D. Xiao, W. Yao, and Q. Niu, Phys. Rev. Lett. **99**, 236809 (2007).

[25] W. Yao, D. Xiao, and Q. Niu, Phys. Rev. B **77**, 235406 (2008).

[26] R. V. Gorbachev, J. C. W. Song, G. L. Yu, A. V. Kretinin, F. Withers, Y. Cao, A. Mishchenko, I. V. Grigorieva, K. S. Novoselov, L. S. Levitov, and A. K. Geim, Science **346**, 448 (2014).

[27] Y. Shimazaki, M. Yamamoto, I. V. Borzenets, K. Watanabe, T. Taniguchi, and S. Tarucha, Nat. Phys. **11**, 1032 (2015).

[28] N. Nagaosa, J. Sinova, S. Onoda, A. H. MacDonald, and N. P. Ong, Rev. Mod. Phys. **82**, 1539 (2010).

[29] Z. Qiao, W. Ren, H. Chen, L. Bellaiche, Z. Zhang, A. H. MacDonald, and Q. Niu, Phys. Rev. Lett. **112**, 116404 (2014).

[30] A. V. Shytov, M. S. Rudner, and L. S. Levitov, Phys. Rev. Lett. **101**, 156804 (2008).

[31] A. F. Young and P. Kim, Nat. Phys. **5**, 222 (2009).

[32] L. E. F. F. Torres, S. Roche, and J. C. Charlier, *Introduction to Graphene-Based Nanomaterials: From Electronic Structure to Quantum Transport* (Cambridge University Press, 2014).

[33] L. Wang, I. Meric, P. Y. Huang, Q. Gao, Y. Gao, H. Tran, T. Taniguchi, K. Watanabe, L. M. Campos, D. A. Muller, J. Guo, P. Kim, J. Hone, K. L. Shepard, and C. R. Dean, Science **342**, 614 (2013).

[34] P. Rickhaus, R. Maurand, M.-H. Liu, M. Weiss, K. Richter, and C. Schönenberger, Nat. Commun. **4**, 2342 (2013).

[35] M.-H. Liu, J. Bundesmann, and K. Richter, Phys. Rev. B **85**, 085406 (2012).

[36] See Supplemental Material for full description of the sample information, electrostatic model, Fabry-Pérot interferences, the Berry phase and quasiparticle tunneling.

[37] A. Logg, K.-A. Mardal, and G. N. Wells, *Automated Solution of Differential Equations by the Finite Element Method* (Springer, 2012).

[38] C. Geuzaine and J.-F. Remacle, Int. J. Numer. Meth. Eng. **79**, 1309 (2009).

[39] M.-H. Liu, P. Rickhaus, P. Makk, E. Tóvári, R. Maurand, F. Tkatschenko, M. Weiss, C. Schönenberger, and K. Richter, Phys. Rev. Lett. **114**, 036601 (2015).

[40] M. Ramezani Masir, P. Vasilopoulos, and F. M. Peeters, Phys. Rev. B **82**, 115417 (2010).

[41] M.-H. Liu and K. Richter, Phys. Rev. B **86**, 115455 (2012).

[42] S. Datta, *Electronic Transport in Mesoscopic Systems* (Cambridge University Press, 1997).

Supplemental Material for

"Tuning anti-Klein to Klein tunneling in bilayer graphene"

Renjun Du (杜人君),[1,*] Ming-Hao Liu (劉明豪),[2,3] Jens Mohrmann,[1] Fan Wu (吴凡),[1,4]
Ralph Krupke,[1,5] Hilbert v. Löhneysen,[1,6] Klaus Richter,[2] and Romain Danneau[1,†]

[1]*Institute of Nanotechnology, Karlsruhe Institute of Technology (KIT), D-76021 Karlsruhe, Germany*

[2]*Institut für Theoretische Physik, Universität Regensburg, D-93040 Regensburg, Germany*

[3]*Department of Physics, National Cheng Kung University, Tainan 70101, Taiwan*

[4]*College of Optoelectronic Science and Engineering, National University of Defense Technology, Changsha 410073, China*

[5]*Institute of Material Science, Technische Universität Darmstadt, D-64287 Darmstadt, Germany*

[6]*Institute for Solid State Physics and Physics Institute, Karlsruhe Institute of Technology (KIT), D-76021 Karlsruhe, Germany*

(Dated: May 2, 2018)

* Renjun.Du@outlook.com

† romain.danneau@kit.edu

I. SAMPLE INFORMATION

In this section, we describe the configuration and geometry of the investigated devices. Fig. S1(a) shows the cross-section of the devices. Bilayer graphene (BLG) or hexagonal boron nitride (hBN) flakes are first exfoliated on substrates with a scotch-tape technique. BLG is characterized by a RENISHAW inVia Raman spectrometer at a wave length of 532 nm (see Fig. S1(b)). The flatness and thickness of hBN flakes are measured by an atomic force microscope (AFM). We then encapsulate BLG between top and bottom hBN flakes, which have the thickness of 14.5 nm and 35 nm, respectively. The hBN-BLG-hBN heterostructure is placed on Si substrate with a 317-nm thick SiO_2 surface layer. Since the dielectric constant of SiO_2 is known to be 3.9, we obtain the dielectric constant for hBN by fitting the slope of displacement field axis, i.e., $C_{\rm tg}/C_{\rm bg} \approx 15.3$, yielding $\varepsilon_{\rm r}^{\rm hBN} \approx 2.2$. We employ e-beam lithography to define a top gate (Ti/Au 5/75 nm) about ~ 150 nm wide, and use the Si substrate as a global back gate. BLG is then contacted from two side edges with metallic leads (Ti/Al 5/85 nm). The contact resistance is estimated from the minimum resistance $R_{\rm min}$ measured in a two-terminal configuration. After subtracting the ballistic resistance $R_{\rm Q} = h/(4e^2 {\rm int}(2W/\lambda_{\rm F}))$ [W is the width of the samples and $\lambda_{\rm F}$ is the Fermi wavelength of charge carriers], we obtain a low contact resistivity $(R_{\rm min} - R_{\rm Q})W/2 \approx 60\,\Omega\,\mu$m [1–3] due to the highly transparent metal-graphene interfaces. All measurements are performed at 4.2 K.

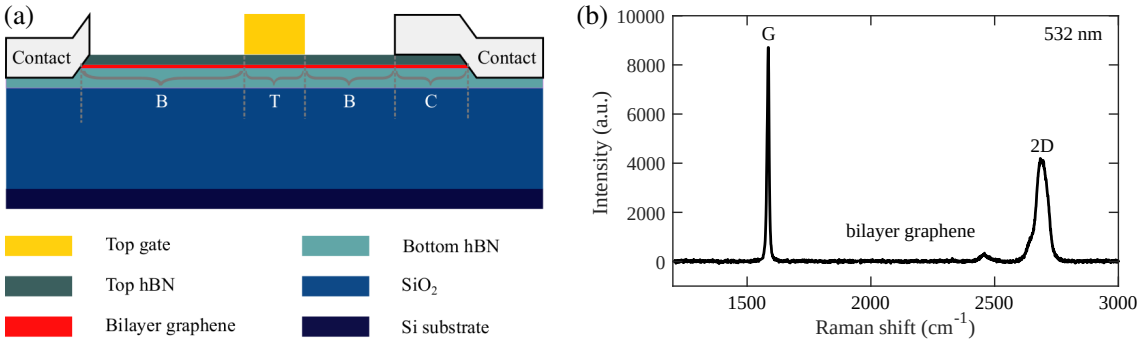

FIG. S1. (a) Cross-section of the investigated devices. (b) Characterization of bilayer graphene: Raman spectrum. Laser wavelength 532 nm, power 2.5 mW, measurement duration 20 s.

Two devices, investigated in this work, have the same W/L ratio of 5 but slightly different channel lengths, i.e., 0.8 µm for device PNJ-A and 1 µm for device PNJ-B. The channel consists of four parts, marked as T (top- and back-gated region), B (only back-gated regions), and C (contact-overlapping region). The geometric parameters of each section are listed in Table SI. The two devices were fabricated with same BLG on one substrate, and during the same run. However,

their measurements were performed in different cool-downs. As a result of thermal cycling, the intrinsic doping of BLG changes.

Sample	Width (μm)	Length (nm)			
		B	T	B	C
PNJ-A	4	310	150	157	181
PNJ-B	5	427	157	235	176
Thickness (nm)	Bottom hBN	Top hBN	SiO_2	Contacts	Top gate
	35	14.5	317	Ti/Al 5/85	Ti/Au 5/75

TABLE SI. The geometric informations of the devices PNJ-A and PNJ-B.

II. ELECTROSTATIC MODEL

Following the experimentally measured device geometry, we construct 2D electrostatic models for PNJ-A and PNJ-B as shown in Fig. S2, where exemplary electrostatic potential distributions are obtained by finite-element-based electrostatic simulation using FEniCS [4] combined with the mesh generator Gmsh [5]. The BLG, together with four metallic electrodes in each model — left contact (cL), right contact (cR), top-gate (tg) and back-gate (bg) — form a linear system of coupled conductors. The carrier density of the BLG sample is given by

$$n(x) = \sum_i \frac{C_i(x)}{e} V_i + n_0(x), \tag{S1}$$

where the electrode label index runs over $i = \mathrm{cL}, \mathrm{cR}, \mathrm{tg}, \mathrm{bg}$, and the self-partial capacitance C_i can be obtained from the electrostatic simulation by treating BLG as the reference conductor [6, 7].

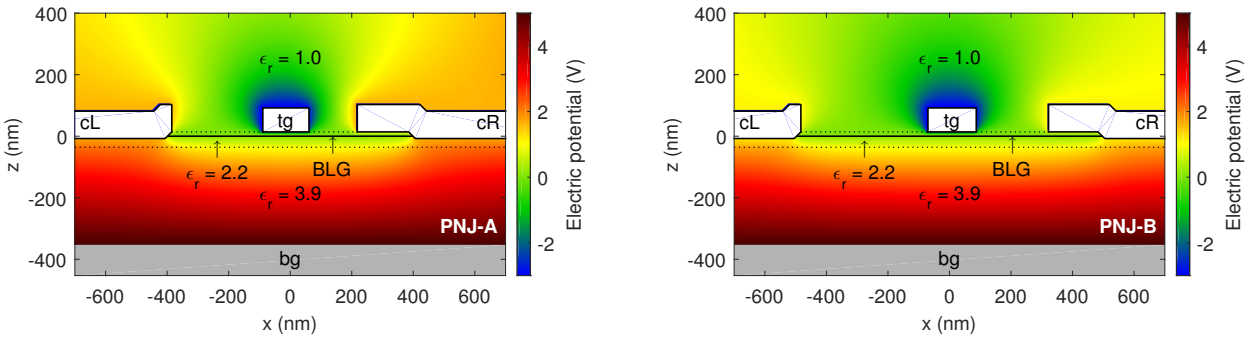

FIG. S2. Geometry of the 2D electrostatic models for the devices PNJ-A and PNJ-B. Exemplary electric potential distributions are obtained by electrostatic simulations, considering gate voltages $(V_{\mathrm{tg}}, V_{\mathrm{bg}}) = (-3, 5)\,\mathrm{V}$ in both devices and effective contact doping potential $V_{\mathrm{cL}} = V_{\mathrm{cR}} = 1.6\,\mathrm{V}$ for PNJ-A and 1.1 V for PNJ-B.

Note that in Eq. (S1), gate potentials $V_{\rm tg}$ and $V_{\rm bg}$ directly correspond to the top- and back-gate voltages in experiments, respectively, while effective potentials $V_{\rm cL}$ and $V_{\rm cR}$ due to contact doping [8], together with the intrinsic doping $n_0(x)$, are to be determined by analyzing the conductance measurement from the experiment, as illustrated in the following.

A. Contact and intrinsic doping

To deduce the effective contact doping potential and the intrinsic doping, i.e., $V_{\rm cL}, V_{\rm cR}$ and $n_0(x)$ in Eq. (S1), we infer the conductance measured as a function of top- and back-gate voltages at zero magnetic field (see Fig. S3), and analyze individually for the two devices in the following.

a. PNJ-A From the Dirac point in region B (DP@B) at $V_{\rm bg} = -1.3\,\mathrm{V}$ shown in Fig. S3(a), a global doping concentration of

$$n_0 = \frac{C_{\rm bg}}{e} \times 1.3\,\mathrm{V} = 6 \times 10^{10}\,\mathrm{cm}^{-2} \tag{S2}$$

can be deduced. For DP@C, we numerically found that the charge neutrality in the C region at $V_{\rm bg} = -26.9\,\mathrm{V}$ can be reached by setting

$$V_{\rm cR} = V_{\rm cL} = 1.6\,\mathrm{V}. \tag{S3}$$

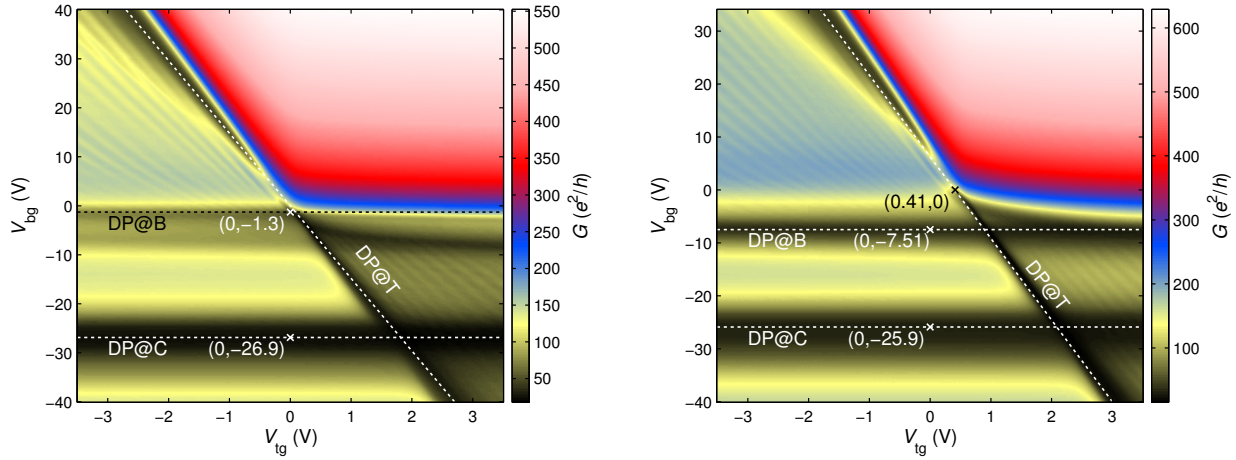

FIG. S3. Analysis of the Dirac point (DP) in different regions of the BLG sample for (a) PNJ-A and (b) PNJ-B from the conductance measurement. Three DP axes indicated by the dashed lines are identified in each panel: DP@B standing for DP in the B region, etc.

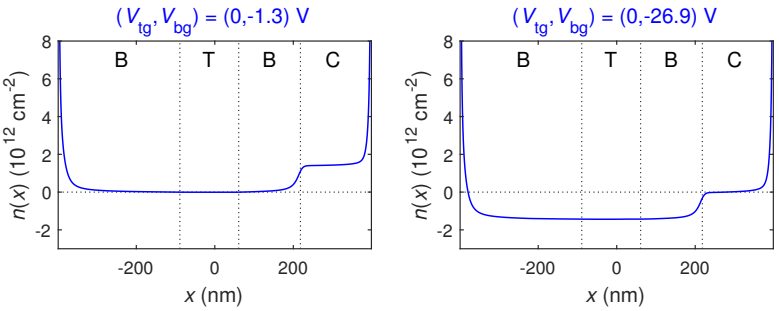

(a) PNJ-A

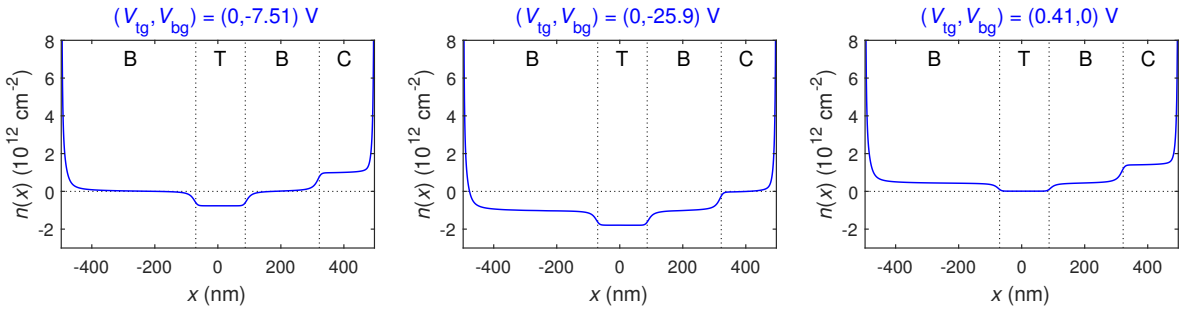

(b) PNJ-B

FIG. S4. Carrier density profiles as a consistency check confirming the contact and intrinsic doping models for PNJ-A and PNJ-B deduced in section II A.

Parameters (S2) and (S3) required in Eq. (S1) complete the electrostatic model for PNJ-A, and are confirmed numerically in Fig. S4(a). Note that a horizontal low-conductance axis below DP@B can be vaguely seen, but is neglected here for simplicity. Together with the fact that the DP@B and DP@T lines in Fig. S3(a) cross each other nearly at $(0,0)$, a constant n_0 seems sufficient to provide a satisfactory electrostatic model. In the following, we will show that a position-dependent $n_0(x)$ model is required for PNJ-B.

b. PNJ-B From the point $(0,-7.51)$ on the DP@B axis of Fig. S3(b), we can deduce a global doping concentration to be

$$n_0 = \frac{C_{\mathrm{bg}}}{e} \times 7.51\,\mathrm{V} = 4.26 \times 10^{11}\,\mathrm{cm}^{-2}\,, \tag{S4}$$

which allows us to reproduce the DP@B axis. Similar to PNJ-A, we found that setting

$$V_{\mathrm{cR}} = V_{\mathrm{cL}} = 1.1\,\mathrm{V} \tag{S5}$$

allows us to reach charge neutrality in the C-region and hence reproduce the DP@C axis. For the DP@T axis, however, the fact that the point $(0.41,0)$ on the DP@T axis is quite distant from

$(0,-7.51)$ on the DP@B axis, suggests a nonuniform doping centered in the T region. To minimize the introduction of additional parameters, let us assume the nonuniform intrinsic doping centered at the T region, called $n_0^T(x)$, to have the same profile as the top-gate capacitance $C_{\mathrm{tg}}(x)$. Let:

$$n_0^T(x) \equiv \frac{C_{\mathrm{tg}}(x)}{e} V_{\mathrm{tg}}^0 \,, \tag{S6}$$

where V_{tg}^0 is the only additional parameter introduced, allowing us to cast $n_0^T(x)$ into a shift of the top-gate voltage, i.e., Eq. (S1) can be now written as

$$n(x) = \frac{C_{\mathrm{tg}}(x)}{e}\left(V_{\mathrm{tg}} + V_{\mathrm{tg}}^0\right) + \frac{C_{\mathrm{bg}}(x)}{e} V_{\mathrm{bg}} + \frac{C_{\mathsf{cL}}(x)}{e} V_{\mathsf{cL}} + \frac{C_{\mathsf{cR}}(x)}{e} V_{\mathsf{cR}} + n_0 \,. \tag{S7}$$

By considering the carrier density in the center of cavity T, say x_T, at the voltage point $(0.41,0)$ on the DP@T axis of Fig. S3(b), we obtain:

$$n(x_T) \approx \frac{C_{\mathrm{tg}}(x_T)}{e}\left(0.41\,\mathrm{V} + V_{\mathrm{tg}}^0\right) + n_0 = 0 \implies V_{\mathrm{tg}}^0 = -0.89\,\mathrm{V} \,. \tag{S8}$$

Model function (S6) with the parameter V_{tg}^0 (S8), together with the uniform part of the intrinsic doping (S4) and the contact doping potential (S5), complete the electrostatic model using (S1), which is explicitly written as (S7) for PNJ-B. As a consistency check, the above doping model is numerically confirmed in Fig. S4(b).

B. Examples of carrier density profiles

Based on the models introduced above, we show examples of simulated carrier-density profiles in Fig. S5, considering top-gate sweeps with back gate grounded in panel (a)/(b) and back-gate sweeps with top gate grounded in panel (d)/(e) for device PNJ-A/B.

Additional examples for PNJ-B are shown in Fig. S5(c) and (f). The former corresponds to the top-gate sweep with back gate fixed at $V_{\mathrm{bg}} = 20\,\mathrm{V}$ considered in Fig. 3 of the main text, while the latter the back-gate sweep with top gate fixed at $V_{\mathrm{tg}} = -1.5\,\mathrm{V}$ considered in Fig. S8(g).

C. Local band offset (on-site energy) profiles

To implement the carrier density profiles $n(x)$ from the electrostatic simulation in transport calculations based on the tight-binding model, we need to translate $n(x)$ into the local band-offset

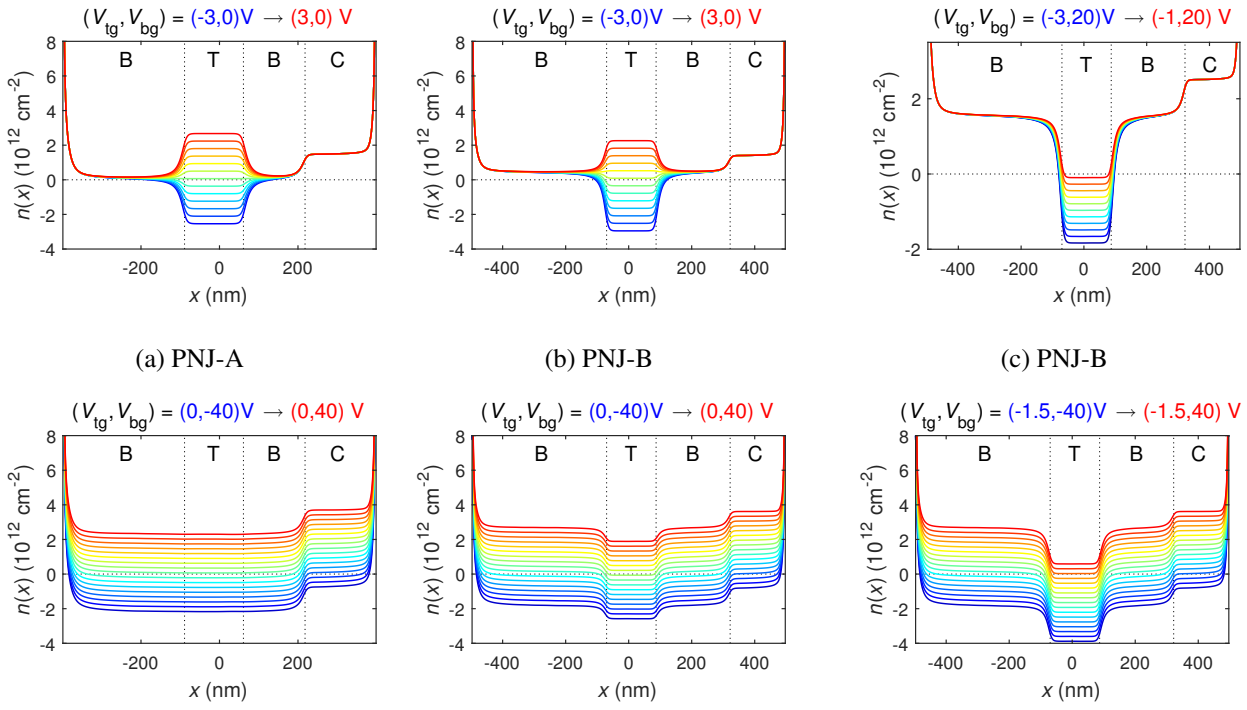

(a) PNJ-A (b) PNJ-B (c) PNJ-B

(d) PNJ-A (e) PNJ-B (f) PNJ-B

FIG. S5. Examples of carrier density profiles from the electrostatic simulation combined with the deduced contact and intrinsic doping described in section II A, showing (a)–(c) top-gate and (d)–(f) back-gate sweeps. Device labels are indicated in each subfigure label. Panels (a,b,d,e) are basic characterizations for both devices. Further examples for PNJ-B are shown in (c) for the top-gate sweep considered in Fig. 3 of the main text and (d) for the back-gate sweep considered in Fig. S8(g).

profile $V(x)$ (also known as the on-site energy profile), i.e., the diagonal elements in the site-resolved tight-binding Hamiltonian:

$$H = H_0 + \sum_i V(x_i) c_i^\dagger c_i \ .$$

In the above expression, the first term H_0 is the pristine part of the BLG Hamiltonian composed only hopping elements, and the second term is the on-site energy with the site index i running over all sites within the considered scattering region and $V(x_i)$ being the energy offset applied on site i.

As already mentioned in the main text, the simulation scheme of the present work is basically the same as that in [9], where a simplified model is considered such that in each region of the simulated BLG device, the carrier density is position-independent, and so are the corresponding asymmetry parameters and on-site energies. In the Supplemental Material (SM) of [9], it was shown how the on-site energy V can be obtained from the gate-controlled carrier density n taking

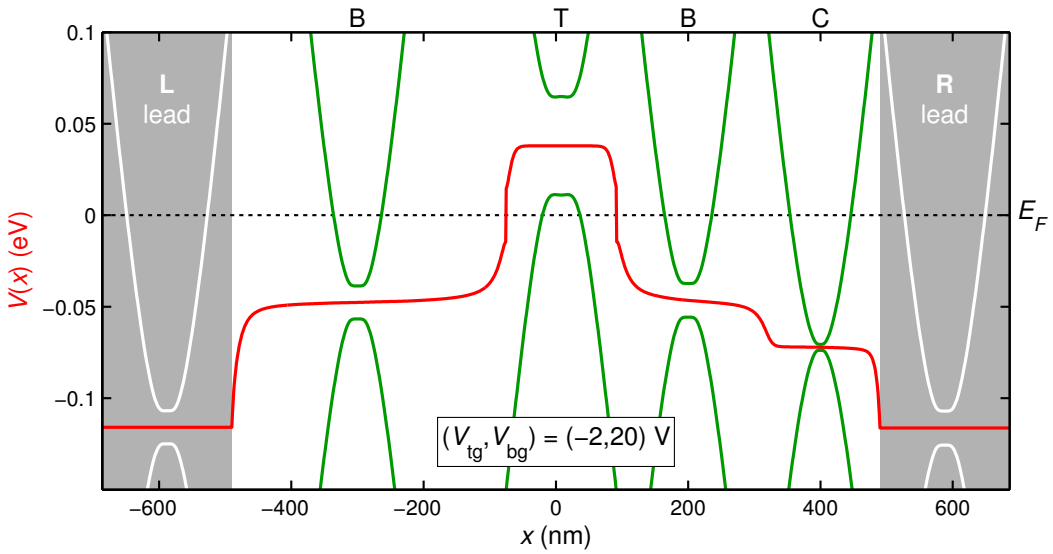

FIG. S6. An example of the on-site energy profile $V(x)$ inferred from the simulated carrier density profile $n(x)$, considering the device PNJ-B at gate voltages indicated above. Local band structures in the B, T, and C regions are sketched in green with the position-dependent band gap [$\approx$ the asymmetry parameter $U(x)$] implemented.

into account the asymmetry parameter U [10]:

$$n \longrightarrow U \longrightarrow V$$

In the present work, we adopt the same method but keep the position dependence of the simulated carrier density $n(x)$, and hence of the corresponding asymmetry parameter $U(x)$ and the resulting on-site energy profile $V(x)$:

$$n(x) \longrightarrow U(x) \longrightarrow V(x)$$

In Fig. S6, we show an example of the resulting on-site energy profile, together with local band structures with the position-dependent $U(x)$ implemented and properly offset by $V(x)$, considering PNJ-B with gate voltages $(V_{\rm tg}, V_{\rm bg}) = (-2, 20)$ V, which is around the center point of Fig. 3(b) of the main text. From the local band structures shown in Fig. S6, it can be seen that the Fermi level is close to the band edge in the T region but far away in the B region. Thus the Berry phase in T is expected to be close to π but close to 0 (or equivalently 2π) in B, like in gapless BLG.

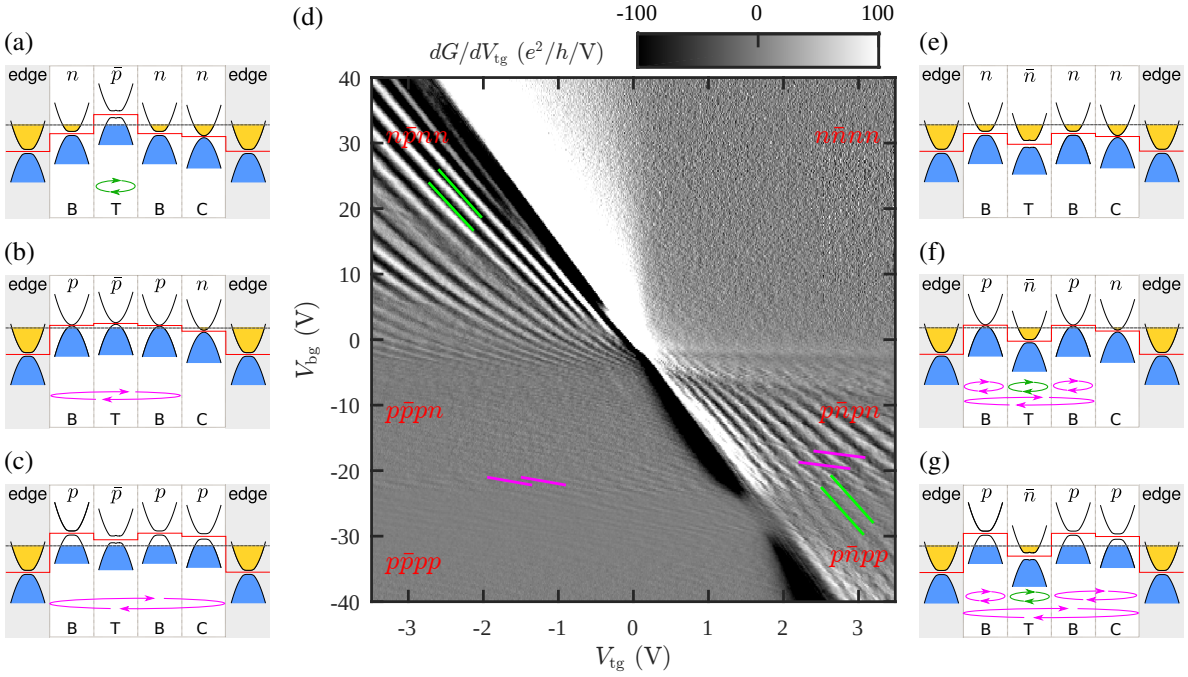

FIG. S7. Sketches of the potential profiles and cavities for the $n\bar{p}nn$ (a), $p\bar{p}pn$ (b), $p\bar{p}pp$ (c), $n\bar{n}nn$ (e), $p\bar{n}pn$ (f), $p\bar{n}pp$ (g) regimes. The red solid line shows the potential profile. The gray dashed line indicates the Fermi level. The green arrows label the FP cavity affected by both top and back gates. The magenta arrows mark the back-gated cavities. (d) Transconductance $dG/dV_{\rm tg}$ as a function of both $V_{\rm tg}$ and $V_{\rm bg}$ for device PNJ-A. The green lines indicate the orientation of the FP fringes tuned by both gates. The magenta lines follow the direction of the fringes tuned by the back gate.

III. FABRY-PÉROT (FP) INTERFERENCES

FP interferences occur when a cavity is formed between two parallel semitransparent *pn* interfaces of a potential barrier [9, 11, 12]. We create the potential barrier across the device by tuning $V_{\rm tg}$ and $V_{\rm bg}$. For better visualizing FP interferences, we show the transconductance $dG/dV_{\rm tg}$ as a function of $V_{\rm tg}$ and $V_{\rm bg}$ for device PNJ-A (see Fig. S7(d)). In the following, we analyze the FP fringes and their formation for each region.

A. FP interferences in the unipolar regime

Resonance in the $n\bar{n}nn$ regime. As presented in Fig. S7(d), FP interferences are absent only in the $n\bar{n}nn$ regime. This absence can be easily understood with the help of the sketch in Fig. S7(e), which portrays the potential profile together with the band diagrams. Except the four regions (B,

T, B and C) of the channel, we also consider the two edges of the device, since these edges are strongly n-doped by the Ti/Al leads, and may lead to two extra pn interfaces at the edges. In the case of the $n\bar{n}nn$ regime, the charge carriers are n-type across the device, therefore, a cavity cannot be generated.

Resonance in the $p\bar{p}pp$ and $p\bar{p}pn$ regimes. Weak conductance resonance is observed in the $p\bar{p}pp$ and $p\bar{p}pn$ regimes (see Fig. S7(d)). The fringes stretch out as marked with the magenta lines. Even though these fringes slightly lean against the horizontal line (CNP) owing to the effect of V_{tg}, dG/dV_{tg} primarily oscillates as V_{bg} varies. We ascribe these fringes to FP interferences in cavities modulated individually by V_{bg}. These cavities develop due to the formation of extra p-n interfaces at the edges of the device, as the magenta arrows shown in Figs. S7(b)–(c). For instance, the entire device becomes a large cavity in the $p\bar{p}pp$ regime (see Fig. S7(c)). Since these cavities are large, both the amplitudes and periods of the resonance are reduced.

B. FP interferences in the bipolar regime

Resonance in the $n\bar{p}nn$ regime. In the bipolar regime, the FP fringes follow the direction of the diagonal line, marked by the green lines in Fig. S7(d). Thus, the resonance arises from a cavity created in T region, labeled by the green arrows in Fig. S7(a). Due to the small cavity, about 150 nm wide, the resonance displays large periods and amplitudes.

Resonance in the $p\bar{n}pn$ and $p\bar{n}pp$ regimes. The FP patterns in the $p\bar{n}pn$ and $p\bar{n}pp$ regimes consist of two sets of fringes. The major one, dispersing along the green lines in Fig. S7(d), originates from the same cavity T as in the $n\bar{p}nn$ regime (see the green arrows in Figs. S7(f)–(g)). The fine resonance marked by the magenta lines, comes from the interferences in three cavities modulated only by the back-gate voltages, as shown by the magenta arrows in Figs. S7(f)–(g). In the case of $p\bar{n}pn$ regime, the sizes of those three cavities are consistent with the lengths of the left B (310 nm), the right B (157 nm) and the entire B-T-B (617 nm) regions, as listed in Table SI. In the case of $p\bar{n}pp$ regime, the three cavities are B (left), B-C, B-T-B-C, and the cavity lengths can be obtained from Table SI. Although the fringe orientations are the same for those three cavities, the periods and amplitudes change due to the different cavity lengths.

IV. SIMULATIONS OF THE BERRY PHASE AND QUASIPARTICLE TUNNELING FOR DEVICE PNJ-B

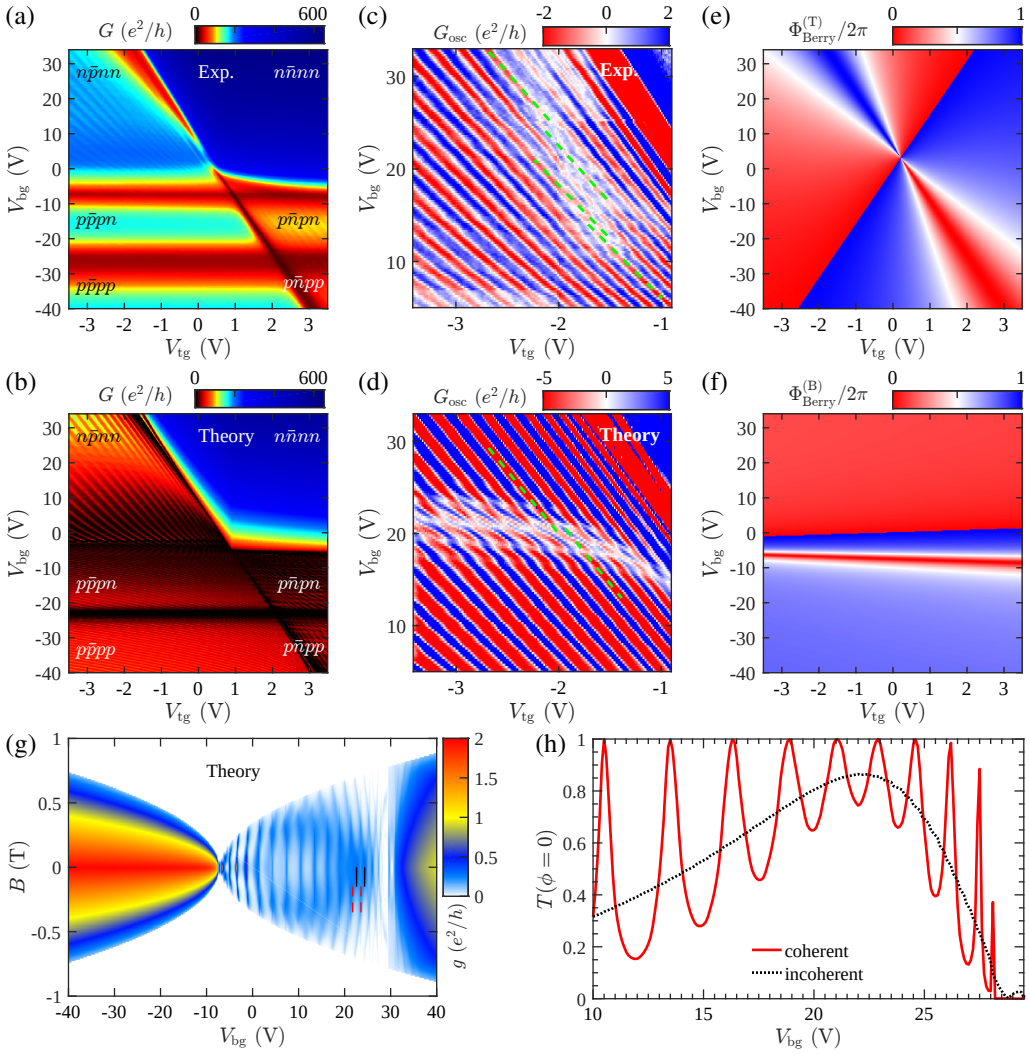

FIG. S8. Conductance measurements (a) and the corresponding simulation result (b) for device PNJ-B at $B = 0$. The oscillating part of the conductance for the experimental (c) and simulated (d) results zoomed in the $n\bar{p}nn$ regime of (a) and (b), respectively. The green dashed lines point out the positions of the phase shifts. The Berry phases in regions T (e) and B (f) evolve with respect to $V_{\rm tg}$ and $V_{\rm bg}$ for device PNJ-B. (g) A numerical example of the conductance g as a function of $V_{\rm bg}$ and B at $V_{\rm tg} = -1.5$ V. The black solid and red dashed lines show the initial and shifted positions of the FP fringes, respectively. (h) The associated transmission probability at normal incidence $T(\phi = 0)$ changes by tuning $V_{\rm bg}$. Two methods, phase coherent and phase incoherent, are used to calculate $T(\phi = 0)$ as displayed by the red and black lines, respectively.

Here, we show more results for the quasiparticle tunneling in gapped BLG. First of all, we

present the characterization of device PNJ-B at 4.2 K and $B = 0$, as the conductance map shown in Fig. S8(a). The corresponding simulation result displayed in Fig. S8(b), corroborates the experimental observation of FP interferences, which is quite similar to that for device PNJ-A. When we examine the oscillating part of the conductance $G_{\rm osc}$ in the $n\bar{p}nn$ regime at $B = 0$, the phase shifts are observed in both experiments and simulations, as highlighted by the green dashed lines in Fig. S8(c) and (d), respectively. These phase shifts are due to the sudden Berry-phase change as discussed in the main text. Comparing Fig. S8(c) and Fig. 4(a) of the main text, we found that the positions where the phase shifts occur, are different. This discrepancy requires further understanding. The Berry phases [13, 14] for regions T ($\Phi^{(\rm T)}_{\rm Berry}$) and B ($\Phi^{(\rm B)}_{\rm Berry}$) are presented as a function of $V_{\rm tg}$ and $V_{\rm bg}$ in Fig. S8(e) and (f), respectively. The Berry phase for T changes with respect to both $V_{\rm tg}$ and $V_{\rm bg}$, while the Berry phase for B only depends on $V_{\rm bg}$.

We show a simulation example of FP interferences under low magnetic fields in Fig. S8(g), where the conductance g varies as a function of $V_{\rm bg}$ and B at $V_{\rm tg} = -1.5$ V. The conductance oscillations exist at $V_{\rm bg}$ in the range of $-7.5 \sim 30$ V , which is in the $n\bar{p}nn$ regime. Instead of tuning $V_{\rm tg}$ as in Fig. 3(a) of the main text, we detect the SLG-like (SLG for single layer graphene) phase shifts of the fringes at $B \approx 100$–200 mT by changing $V_{\rm bg}$. The black solid and red dashed lines in Fig. S8(g) show the initial and shifted positions of the FP fringes, respectively. The half-period shift occurs at $V_{\rm bg} \approx 22$ V, indicating the Berry phase of π is picked up in region T. The corresponding transmission probability at normal incidence $T(\phi = 0)$ is calculated for two cases, phase coherent and phase incoherent, shown as the red and black curves in Fig. S8(h), respectively. Here, we found the transition from broken anti-Klein [9] to nearly complete Klein tunneling as in the main text when $V_{\rm bg}$ declines from 29 V to 10 V. The maximum of $T(\phi = 0)$ is 0.86 at $V_{\rm bg} = 22$ V. For $V_{\rm bg} < 22$ V, $T(\phi = 0)$ drops to 0.32, in contrast to 0.65 obtained in Fig. 3(i) in the main text. Therefore, the recovery of anti-Klein tunneling at high Fermi energies is improved, since the Berry phases in B and T are both closer to 0 (or equivalently 2π).

[1] L. Wang, I. Meric, P. Y. Huang, Q. Gao, Y. Gao, H. Tran, T. Taniguchi, K. Watanabe, L. M. Campos, D. A. Muller, J. Guo, P. Kim, J. Hone, K. L. Shepard, and C. R. Dean, Science **342**, 614 (2013).

[2] V. E. Calado, S. Goswami, G. Nanda, M. Diez, A. R. Akhmerov, K. Watanabe, T. Taniguchi, T. M. Klapwijk, and L. M. K. Vandersypen, Nat. Nanotech. **10**, 761 (2015).

[3] M. Ben Shalom, M. J. Zhu, V. I. Fal'ko, A. Mishchenko, A. V. Kretinin, K. S. Novoselov, C. R. Woods, K. Watanabe, T. Taniguchi, A. K. Geim, and J. R. Prance, Nat. Phys. **12**, 318 (2016).

[4] A. Logg, K.-A. Mardal, and G. N. Wells, *Automated Solution of Differential Equations by the Finite Element Method* (Springer, 2012).

[5] C. Geuzaine and J.-F. Remacle, Int. J. Numer. Meth. Eng. **79**, 1309 (2009).

[6] D. K. Cheng, *Field and Wave Electromagnetics*, 2nd ed. (Prentice Hall, 1989).

[7] M.-H. Liu, Phys. Rev. B **87**, 125427 (2013).

[8] M.-H. Liu, J. Comput. Electron. **12**, 188 (2013).

[9] A. Varlet, M.-H. Liu, V. Krueckl, D. Bischoff, P. Simonet, K. Watanabe, T. Taniguchi, K. Richter, K. Ensslin, and T. Ihn, Phys. Rev. Lett. **113**, 116601 (2014).

[10] E. McCann and M. Koshino, Rep. Prog. Phys. **76**, 056503 (2013).

[11] A. F. Young and P. Kim, Nat. Phys. **5**, 222 (2009).

[12] P. Rickhaus, R. Maurand, M.-H. Liu, M. Weiss, K. Richter, and C. Schönenberger, Nat. Commun. **4**, 2342 (2013).

[13] M. V. Berry, P. Roy. Soc. Lond. A Mat. **392**, 45 (1984).

[14] D. Xiao, M. C. Chang, and Q. Niu, Rev. Mod. Phys. **82**, 1959 (2010).